EXPERIMENTAL INVESTIGATION OF UNSTEADY INTERACTION OF SECONDARY FLOWS IN A TURBINE STAGE

L. M. Aurahs, M. G. Rose, S. Staudacher,
Institute of Aircraft Propulsion Systems, University of Stuttgart, Germany

Abstract

This paper presents detailed flow visualization photographs and post-processed results of the interaction of the vane secondary flows with each other and with the rotor of an axial water flow turbine model. Vortex breakdown has been experimentally observed inside the rotating passage of the turbine blade. A further breakdown mechanism of the von Kármán vortex street and its downstream development in the secondary flows accumulation area of the vane exit close to the hub has been investigated. The measurements were taken in a vertical water channel with ink injection for flow visualization and hydrogen bubbles for local velocity measurement. With these techniques streak lines, particle paths and time lines were introduced into the flow field to gather quantitative as well as qualitative data. For an isolated investigation of the von Kármán vortex street measurements in a water cascade were conducted.

For different relative positions of rotor to stator a series of photographs were taken. With an image editing process the RMS of the pictures' pixel values was calculated for discrete rotor-stator relative positions to extract and identify transitional nondeterministic behavior of the flow field. A photogrammetric approach was used to gain insight into the apparent velocity field.

A frequency analysis revealed a periodic changing breakdown behavior of the involved vortices. This behavior is not uniform and the different vortices show a phase shift in their breakdown processes.

1. NOMENCLATURE

AF		absolute frame of reference
c	[m/s]	local velocity, vortex axial velocity
d	[m]	arbitrary distance
δ	[m]	boundary layer thickness
f	[1/s]	shedding frequency
h	[m]	NGV trailing edge thickness
HSV		Horse Shoe Vortex
NGV		Nozzle Guide Vane
ρ	[kg/m³]	density
Re		Reynolds number
RF		relative frame of reference
RMS		root mean square
S		Swirl number
Sr		Strouhal number
s	[m]	vane chord length
T	[s]	blade passing period
u	[m/s]	rotor (vortex) circumferential velocity
ν	[m²/s]	kinematic viscosity
VKVS		von Kármán Vortex Street
Φ		streamline helicity
ω_{ij}	[1/s²]	rotation tensor

2. INTRODUCTION

It is commonly accepted, that secondary flows in turbine stages are a cause of losses. Various researchers investigated the development and shedding of secondary vortices in turbine guide vanes ([1], [2]) and tried to reduce the subsequent losses by adapted end wall and blade design. Since these attempts result in noticeable secondary loss reduction for the stator and improvements of stage efficiency from 0.2% up to 1.0% so far, unsteady flow features of interaction between stator and rotor flow field are in the focus of recent research. Such features are vortex wake interaction ([3], [4]), the interaction between vortices and blades [5] and the time varying vortex breakdown phenomena, the focus of the current investigation.

Early theoretical work on vortex breakdown in steady flows (e.g. [6], [7]) has been focused on the prediction of the exact breakdown location depending on imposed conditions and the downstream post breakdown vortex behavior. On inclined delta-wings, the manner of vortex propagation has a profound impact on the pressure distribution and therefore on the wing's lift ([7], [8]). In the investigations of [8] the appearing vortex breakdown structure was described as a spiral breakdown mode whereas the same flow conditions resulted in a bubble mode breakdown of the vortex as well. Later research, using the more controlled conditions of a pipe flow, such as [9], has shown that the mode of evolution and breakdown location depends strongly on the vortex Swirl number and Reynolds number. The experiments of [10] revealed that with an increasing Swirl number, a late spiral mode breakdown changes to an earlier single bubble mode and then a multi bubble mode, adding a spiral breakdown until it reaches the state of a further upstream spiral breakdown mode, respectively.

In a turbine flow environment, the changing pressure field imposed by the rotor and other unsteady flow features, such as the von Kármán vortex street, dominates the instability behavior of the secondary flow vortex shedding. In such a flow regime, the investigations of [11] show a region of high turbulence inside the rotor passage in the vicinity of blade pressure side close to the leading edge. This was referred to as a result of the NGV wake interacting with the blade's leading edge. Focusing on this very area, further investigations of [12] and [13] revealed

various vortex breakdown modes of the passage vortex and the horse shoe vortex, changing with the periodically passing rotor pressure field. Investigations on vortices in conical diverging pipes such as [14] showed that imposing an adverse pressure gradient has a destabilizing effect on vortices and can shorten the distance from initiation to breakdown of the vortex. The experiments of the presented research show the vortical structures of the horseshoe vortex, the passage vortex and the von Kármán vortex street as they interact with the rotor flow field inside the water rig turbine stage. This paper addresses the unsteady flow condition resulting in the different breakdown phenomena inside the turbine stage.

3. EXPERIMENTAL APPARATUS

3.1. Facility

The experiments were conducted at the vertical water channel, explained in [12] und [2] in more detail. At the vertical test facility, the throughflow of the turbine stage is top down. All depicted images of the turbine are turned 90° to the left to provide a familiar view of the turbine stage flow field. The vane chord length based Reynolds number $Re=c_{out} \cdot s_{NGV}/\nu$ is 35,000 for the main measurement results. For a sensitivity analysis on flow condition changes, the Reynolds number is increased to 70,000 by adjusting inlet flow velocity and rotational speed accordingly to match Re levels relevant for jet engine turbine stages. The blade Reynolds number, based on the same arguments, is about 22,850 and 45,700 respectively. The hub inlet body (Fig.1) is parabolic with a cylindrical hub wall length of 0.662m to the NGV inlet. This results in a measured hub boundary layer thickness of approx. δ=9mm (δ=7mm for Re_{NGV} = 70,000) at the NGV inlet. The shroud side boundary layer thickness is approx. 11mm (8mm for Re_{NGV} = 70,000), however, the associated secondary flow features close to the casing are not investigated.

Some operating conditions and the main geometrical parameters are listed in Table 1.

	Vane (tip- hub)	Rotor (tip- hub)
number of blades	24	32
blade span [mm]	110	109
mean inlet flow angle [deg]	0	46.4
exit flow angle [deg]	19.5 - 21.5	69.8 -69.2
flow coefficient c_{ax}/u[-]	-	0.542
stage loading $\Delta h/u^2$ [-]	-	1.089
Reynolds number [-]	35,000 (70,000)	22,850 (45,700)
axial chord length [mm]	70	56,5
aspect ratio [-]	1,57	1,946
solidity [-]	1,23	1,32
axial gap/NGV axial chord length [-]	0,357	-

Table 1. Turbine stage specification

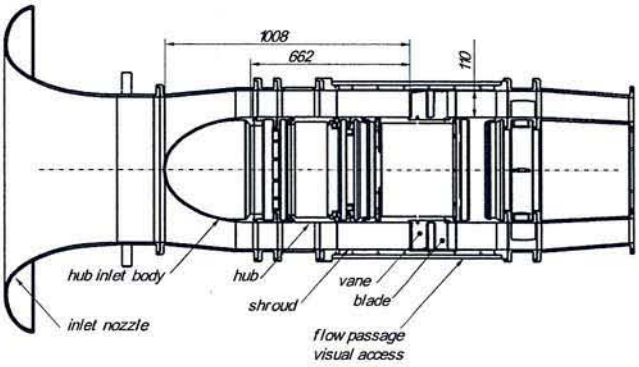

Figure 1. Side view of the water rig turbine stage

The fluid used is pure tap water without any anti-corrosion additives or additional electrolytes to enhance hydrogen bubble production at the cathode wires. The water temperature is constantly measured and flow speed and rotational speed are adapted to sustain a constant Reynolds number.

3.2. Visualization Methods

The used methods for flow visualization are ink injection and cathode wires to produce hydrogen bubbles. With these techniques streak lines, particle paths and time lines were introduced into the flow field to gather quantitative as well as qualitative data.

The ink injection system as well as the camera system is described in [12] in more detail. The ink is injected through holes of 0.8 mm in diameter at the hub side passage close to the NGV pressure side and in front of the leading edge, as shown in Fig. 2. Each injection hole is connected with a separate valve to adjust ink supply pressure for an adequate flow rate. The hole blowing ratio is negligible.

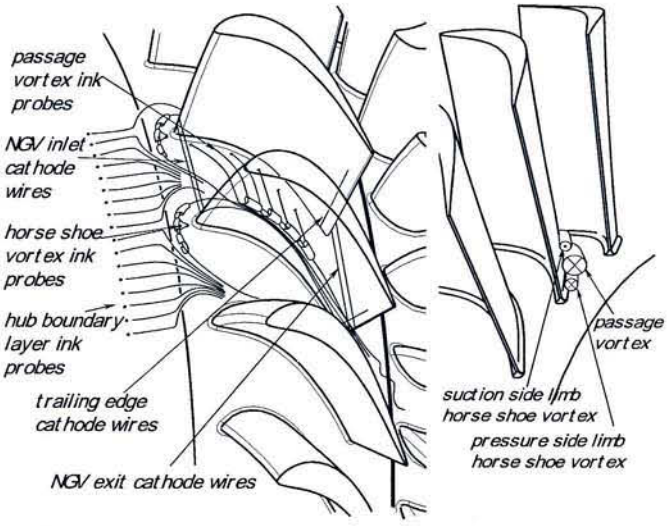

Figure 2. Cathode wire/ink probe positioning and secondary flow feature traces

The hydrogen bubbles are generated via cathode wires of 25µm diameter. The positioning of these wires is shown in Fig.2. By a rectangular pulsing of the voltage, timelines allow visualization of the velocity profiles and even into small turbulences. Additionally the hydrogen bubbles are

preserved as discrete objects throughout the flow field of interest until they dissipate into the water, whereas ink results in a diffuse dispersion after a vortex instability or turbulence onsets.

For the hydrogen bubbles, which are approx. of the same diameter as the cathode wire, friction or shear stresses with the fluid dominate the bubble motion over buoyancy. The ascension of the bubbles with a diameter of d=25µm is approx. $3.5 \cdot 10^{-4}$m/s which is approx. 0.17% of the mean inlet velocity and therefore negligible. The local Reynolds number based on the wire's diameter Re_d =5 is below that, needed for the wire to effect a von Kármán vortex street [15] but higher than Re<<1 needed for a Stokes flow. Therefore, the cathode wire forms a wake which results in a slower motion of the hydrogen bubbles than the actual local flow velocity. To compensate, a correlation, following [16]

$$(1) \quad c = \frac{c_b}{1 - k\sqrt{d / x}}$$

with c_b as the appearing bubble velocity, d as the diameter, x ($x>k\sqrt{x}$) as the distance of the bubbles to the wire and k as a parameter which is suggested to be approx. 1,3 for $3<Re_c<40$, can be used. This was done to extract the profile of the incoming boundary layer and local velocities for comparison with CFD results.

3.3. Data Acquisition

The camera and triggering system are described in [12] in more detail. For the presented measurements a further camera was added to gather information about the flow features' exact location in spanwise direction by a photogrammetric approach.

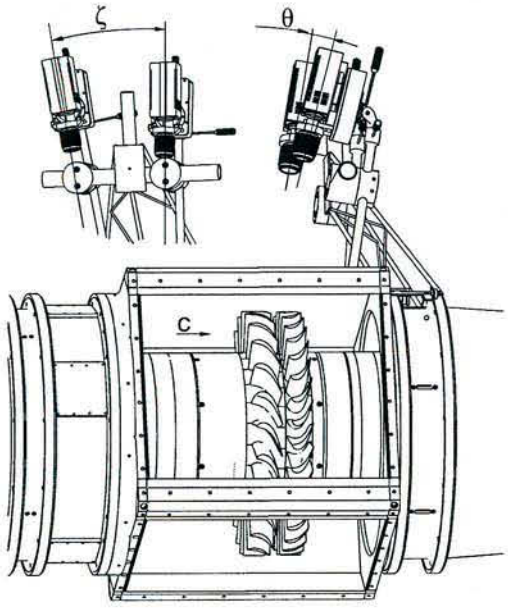

Figure 3. Camera positioning at the test rig, flow direction from left to right

The second camera is aligned with an angle shift vertically (θ) and horizontally (ζ) according to Fig.3. For a two-dimensional picture distances and objects, comparing them with the hub reference grid, appear bigger the closer they are situated to the cameras, whereas their position in radial direction is not known. So even for a qualitative interpretation of the flow field, the stereoscopic approach is inevitable. The cameras are mounted on a circular slide for a rotor passage alignment to avoid the obscuring of the field of interest by the neighboring blades.

To localize and identify the vortex breakdown, the picture pixel RMS analysis described in [12] was used to emphasize the vortex region of the highest non-deterministic signature. The pixel RMS values are calculated according to

$$(2) \quad RMS_{pixel} = \sqrt{\frac{\sum (pixel_{values} - AV)^2}{n_{photographs}}}$$

with $pixel_{values}$ as a single photography, AV stands for the averaged pixel values of all used pictures of this particular time step and $n_{photographs}$ as the number of pictures used.

With a trigger system, a picture series of a distinct rotor relative position were taken and post-processed with the pixel RMS approach. The NGV passage as well as the rotor passage are labeled equally spaced as seen in Fig.4. The spacing of the scale in Fig.4 is 5mm. Since the vane blade ratio is ¾ one has to bear in mind that discussing flow features in the absolute frame or in the relative frame, the use of two different cycle durations is possible. On the one hand, watching the wake of an NGV interfering with the rotor pressure field, the period of the absolute frame T_{AF} is pivotal. On the other hand, focusing on the very area in the front part of the blade passage (approx. after ¼ of the chord length) the breakdown phenomena occur periodically in the relative frame of reference time interval (i.e. the blade passing period T_{RF}). In this paper, $0 \leq t/T_{AF} \leq 1$, segmented into nine discrete intervals, is used to define the rotor relative position.

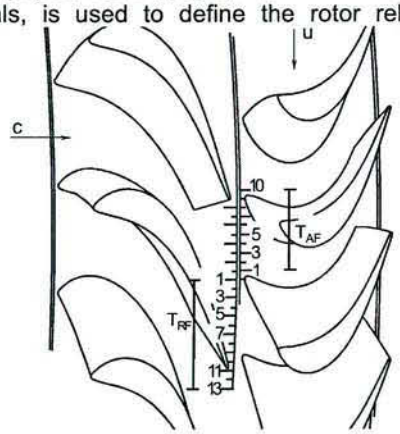

Figure 4. Labeling of rotor relative frame and absolute frame of reference, $0 \leq t/T_{AF} \leq 1$

The reduced spiraling frequency (i.e. Sr) of the vortices and the shedding frequency of the VKVS are extracted from the pictures by measuring the distance between the spiraling arms of the vortices and the distance between the vortices respectively. According to

$$(3) \quad Sr = \frac{f \quad h}{c} = \frac{h}{d} \quad \text{, with} \quad c = f \quad d$$

and h for the trailing edge thickness, d for the measured distance between the eddies, the Strouhal number can be calculated by geometrically measured magnitudes.

In order to judge if a critical state of a vortex is reached, the streamline helicity according to

(4) $\Phi = arctan\frac{u}{c}$

is extracted. Thereby, c is the axial velocity and u stands for the circumferential velocity of the vortex. For the circumferential velocity, the maximum value of u is used. A vortex state with a streamline helicity Φ of more than 50° is commonly regarded to be supercritical. The streamline helicity can easily be gained from the numerical data. In the experiment, the angle Φ can be measured directly from the pictures if the dye streaks can still be identified as discrete lines as they trace the vortex. The more common comparison of the swirl number S or the circulation number Ω is of no use, since they are nondimensionalized by a length scale, usually a tube diameter.

4. CFD

The additionally used CFD provides data about the time-resolved pressure field and the vortices' attributes in the steady flow field of the NGV. From experience, the numerical prediction of these features is very reliable. The commercial code CFX was used. The computation was performed with a fully implicit second order scheme. No turbulence models were used, so the calculation was purely laminar. In the experiments the earliest turbulence onset was after the vortices breakdown inside the rotor passage. So for a pre vortex-breakdown prediction of the flow, the assumption of a laminar flow is adequate. One NGV flow passage is meshed unstructured with 4.5 million grid nodes with boundary layer prisms (y^+=1.2) and reduced resolution of the vane trailing edge. This prevents the prediction of the von Kármán vortex street. The mesh has local refinements based on experience gained from the water rig experiments. The CFD calculations are time-resolved with a sliding plane at the NGV exit to allow vortex structures formed in the NGV pass the mesh interface. However, the mesh used was not capable to predict vortex breakdown.

5. RESULTS

The traces of the downstream propagating vortices originating from the NGV passage are depicted in Fig.2. The vortices' location at the NGV exit is already known from previous investigations for lower Reynolds number [13]. For the higher Reynolds number flow conditions (Re_{NGV} = 70,000) these positions as well as the whole vortex traces have not changed noticeably except for the slightly further extended backflow region in front of the leading edge at the hub. The right hand side depiction of Fig.2 shows the vortices' location at the exit of the NGV passage. The passage vortex as well as the horse shoe vortex pressure side limb have a negative sense of rotation whereas the suction side limb HSV has a positive sense of rotation, relative to the viewers plane.

In some experiments, such as [2], a flow pattern is observed with the passage vortex and the pressure side limb horse shoe vortex merging in the rear part of the NGV and appearing as one bigger vortex in the NGV exit. However, in the experiments presented, each vortex shows a separate behavior in their breakdown process and frequency behavior [13].

5.1. Reduced Frequency Analysis

This frequency analysis, using Sr as the reduced frequency, treats the spiraling frequency of the vortices and the shedding frequency of the VKVS over one blade passing period. For this analysis 100 pictures of each rotor relative position were used to extract the vortices' swirling frequencies and the measurement's standard deviation.

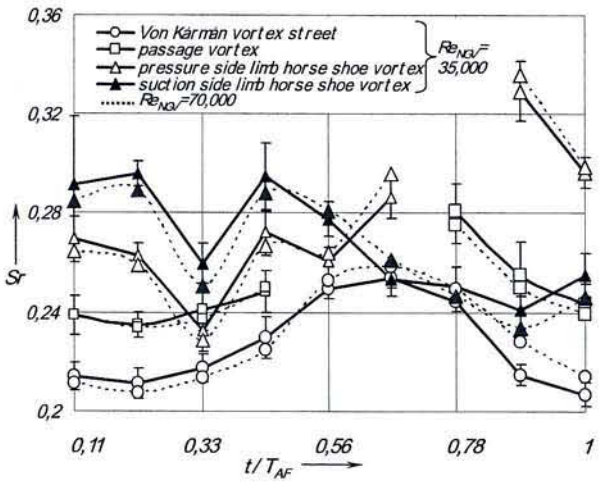

Figure 5. Strouhal number vs. blade passing period

The interrupted Sr curves (e.g. passage vortex Fig.5) show a state of an early breakdown with a turbulent post-instability behavior, in such a way that no spiraling frequency can be observed.

For Re_{NGV}=35,000 the secondary vortices' unsteady frequency behavior in Fig.5 has already been discussed in [13]. For the higher NGV based Reynolds number of 70,000 the sinusoidal change of the VKVS shedding frequency is slightly amplified. In principle, the frequency behavior of the vortices and their early breakdown occurrence at a distinct rotor relative position does not change. The differences in Fig. 5 between the curves for the vortices' Strouhal number for Re_{NGV} = 35,000 and Re_{NGV} = 70,000 are largely well inside the measurements standard deviation.

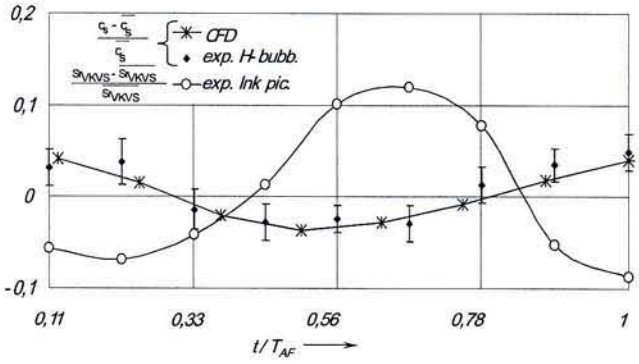

Figure 6. Relative change of Sr and the velocity differences at the measurement location for the chart of Fig. 5 (Re_{NGV}=35,000). Velocity gained by hydrogen bubble flow vis. and CFD

Fig. 6 shows the change of the VKVS Strouhal number relative to the Sr averaged over a full blade passing

period. This is qualitatively the same as the VKVS Strouhal number shown in Fig.5, however with lower amplitude. The other curve of Fig.6 stands for the relative change in velocity at a sample line closely behind the NGV trailing edge at 20% span in radial direction. The velocity data are obtained from CFD results and checked by hydrogen bubble measurements. The measured velocity changes are given with their deviation to take the unsteady nondeterministic flow field at the measurement location into account. The velocity measurements obtained from the hydrogen bubble visualization give the same trend as the velocity data from the numerical result. Bearing in mind that an increasing velocity at constant shedding frequency of the VKVS results in more distanced eddies at the axial gap and therefore yields a lower Strouhal number, this could well be an explanation for the pronounced sinusoidal shaped Sr behavior of the VKVS, given by [13] and Fig.5. However, the spiraling frequency changes of the other vortices shown in Fig.5 can not be explained by this change in velocity.

The amplitude of the relative velocity change in Fig.6 is smaller than the amplitude of the relative Sr change. The measured eddy distances for the Sr investigation of the VKVS are integral results of the velocities. So one can assume the observed Sr change of the VKVS is mainly to the velocity change. Therefore the Sr levels of the vortices swirling frequency in Fig.6 can be corrected by substraction of the VKVS Strouhal number deviation around its mean value.

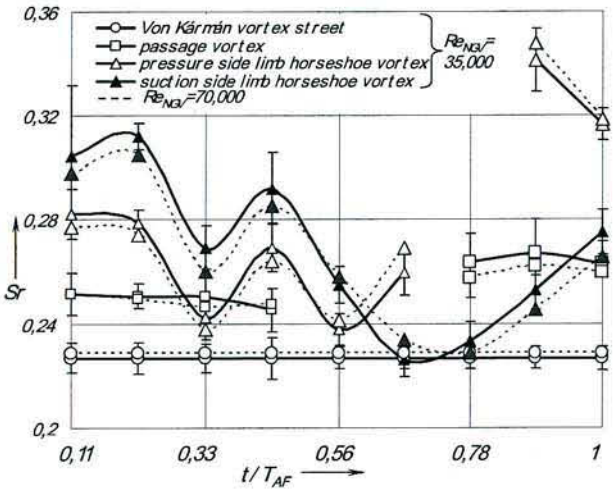

Figure 7. Strouhal number corrected by VKVS Sr of the accoding Re number vs. blade passing period

In Fig.7, the corrected Sr values of Fig.5 are presented. The Sr curves of the VKVS for Re = 70,000 and Re = 35,000 therefore show their mean values. Please notice that these values are corrected by the VKVS Sr levels of the according Reynolds number.

5.2. Observed Breakdown Modes

The breakdown modes observed for the HSV pressure side limb are of spiral type, of double helical type and occasionally of bubble type breakdown mode for Re_{NGV}=70,000.

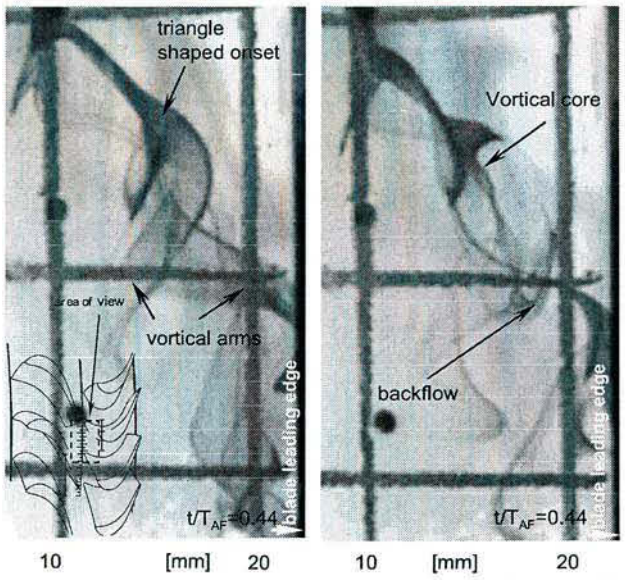

Figure 8. Dye streak visualization of double helix (left) and bubble mode breakdown (right) of the HSV pressure side limb for t/T_{AF}=0.44

In [13] an early bubble type breakdown of the pressure side limb of the horse shoe vortex was reported to be the more common breakdown. For the present Reynolds number (i.e. Re_{NGV}=70,000), a spiral vortex instability and a double helix instability were observed more often. Fig.8 shows two breakdown modes of the horse shoe vortex pressure side of the same rotor relative position t/T_{AF}=0.44. Both the double helix (left hand side) and the bubble (right hand side) are of distinct shape. The depicted bubble shows an inner core vortex and the backflow region as the ink is transported from the core back along the bubbles' hull. This picture matches the dye visualization picture of a bubble vortex breakdown in a tube flow condition given by [17].

Such a bubble mode breakdown is reported to occur mainly in axisymmetric flow conditions like in tubes [18] since the bubble mode breakdown itself has an inherent axisymmetric flow structure. However, again, a clear bubble type structure was observed only at five out of 100 pictures. Mostly, the pressure side limb HSV is observed as it evolves from an initial spiraling instability to a double helix breakdown, as shown in Fig.9.

In Fig.9 for t/T_{AF}=0.22 one can see the typical triangular shaped ink dispersion of a double helix instability onset. Throughout the blade passing period, the vortex instability onset for the initial spiraling behavior has a fixed location about 10mm behind the NGV trailing edge. The bifurcation of the double helix gains strength and moves downstream (compare Fig.9 for t/T_{AF}=0.22 to t/T_{AF}=0.44).

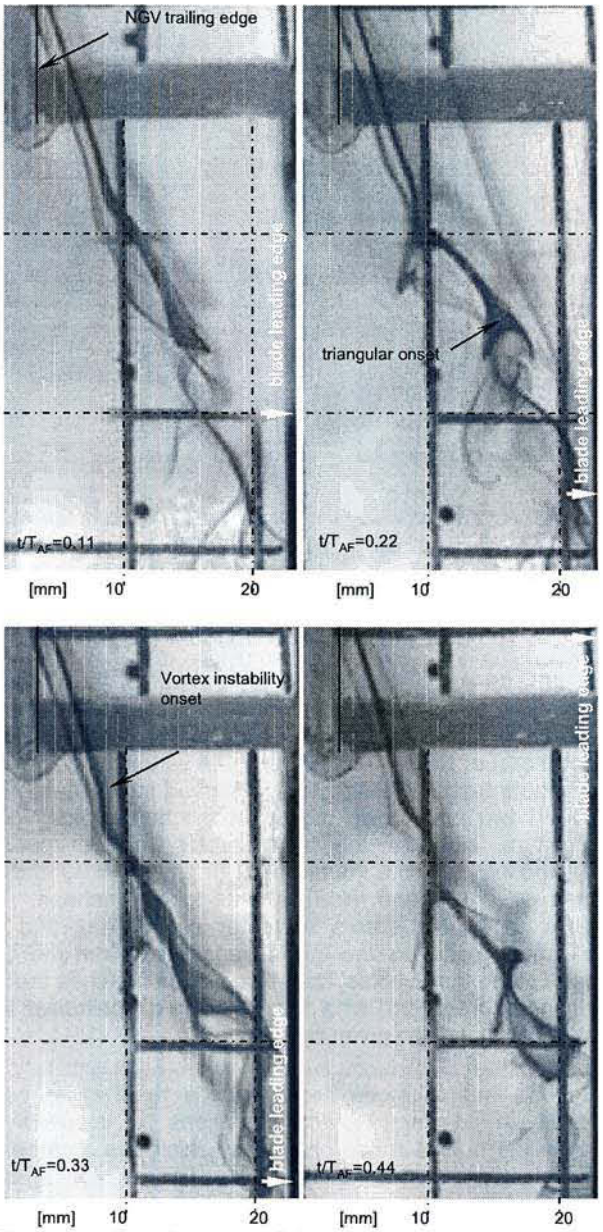

Figure 9. Development of the spiral vortex breakdown of the pressure side limb HSV

For the passage vortex, neither the experimental ink pictures of the dye filaments nor the numerical velocity data showed a critical value of the streamwise helicity Φ of the vortices before breakdown. These values were between $\Phi \approx 12°$ for $t/T_{AF} = 0.11$ to $\Phi \approx 28°$ for $t/T_{AF} = 0.77$. The experimental results of the streamwise helicity, according to eqn. (4) showed a critical state of the vortices only after initiation of the double helix breakdown and the bubble mode breakdown of the passage vortex and the HSV pressure side limb. Since the numerical solution was not capable to predict the vortex breakdown behavior, the earliest state with a critical value of Φ was a result of the interaction of the vortex branches with the blades leading edge which results in a local transverse reorientation of the vortex [19].

In the present experiments, instead of an early bubble mode breakdown which prevented an interpretation of a spiraling frequency analysis of the vortex post instability behavior, strong interaction of the HSV pressure side limb with the Von Kármán vortex street resulted in strong diffusion of the ink.

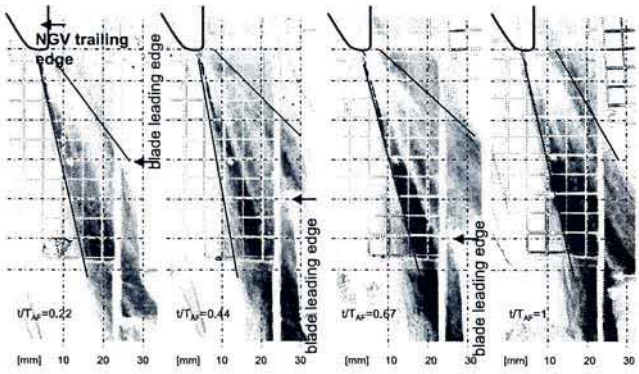

Figure 10. Inverted RMS signature of VKVS broadening for different rotor relative position (dark stands for high unsteadiness)

For the rotor relative position of $t/T_{AF} = 0.66$ (Fig.10) the VKVS broadens in circumferential direction, when the rotor blade pressure field imposes an increasing positive pressure gradient inside the axial gap along the VKVS trace. This can be seen as a skewing towards the following blade suction side as well. The same effect of VKVS dislocation can be seen in the CFD data given by [4]. The high frequency pressure field and the velocity field of the VKVS results in a nondeterministic behavior or even triggers breakdown processes in the vortices as they interfere more strongly with the VKVS. However the used camera setup did not provide an adequate resolution to capture and confirm such a feature.

6. DISCUSSION

The passage vortex breakdown in the turbine's flow regime discussed has been identified already in [12] with a pixel RMS procedure. In [12] and [13] breakdown modes have been identified as bubble type, spiral type and, occasionally, a double helix type [12]. In [13] the behavior and transition of the different breakdown modes into another breakdown type has been discussed. The unsteady behavior is, as a Strouhal number investigation revealed, influenced by the Von Kármán vortex street and by the current rotor relative position and its pressure field. The ambiguity mentioned in [13] about the reduced frequency analysis and the bubble mode and double helix mode breakdown can now be cleared up. Comparing the reduced mean velocity differences from the sample location (i.e. the same location as the measurements for the frequency analysis of Fig.5) one can see that the increasing and decreasing velocity at the axial gap between stator and rotor is no explanation for the corrected Sr run of the passage vortex and the horse shoe vortex in Fig.7 as it is for the VKVS.
The experimental and numerical results for Φ are vague. However, the quintessence of this approach is the by far lower streamwise helicity as it would be expected for a vortex breakdown in a steady flow regime. So one might assume the necessity of the unsteady flow field of the rotor to cause vortex breakdown of the observed NGV related secondary flow vortices. This still has to be confirmed by precise quantitative experimental velocity data of the flow features.

The statement about the evolution of vortex breakdown phenomena depending mainly on the vortex swirl and its Reynolds number (e.g. [10]), are based on investigations with controlled and quiet flow conditions. For a turbine environment these flow conditions are more stochastic since the shedding frequency of the VKVS does not comply with the rotor passing frequency. On the other hand, the graph of Fig.5 reveals an over-all periodic behavior of the initial spiraling instability of the vortices, their breakdown and strong interference with the VKVS in average. This is not self-evident, since an external imposed adverse pressure gradient is not indispensible for breakdown initiation.

Even for an externally imposed positive pressure gradient along the vortex, the overall pressure gradient can be negative due to the induced pressure gradient of the vortex swirl. Following [17] for an inviscid flow the local pressure gradient forms to

$$(5)\quad \left.\frac{dp}{dx}\right|_0 = \left.\frac{dp}{dx}\right|_\infty + \rho \int_0^\infty \frac{\Gamma v}{u r^3}\frac{\partial \Gamma}{\partial r} dr$$

with r as radial direction originating from the vortex core, u as vortex circumferential velocity and Γ as circulation. So even for the accelerating flow at the rear part of the NGV passage, vortex breakdown can be initiated if the swirl induced pressure gradient along the vortex axis prevails.

However, the initiation of the spiraling for the passage vortex, the suction side limb of the horse shoe vortex [13], and the HSV pressure side limb, as seen in Fig.9, has a fixed location. Whereas the initiation of the instability modes, leading to a rapid subsequent breakdown, varies in location depending on the rotor relative position.

Doubling the Reynolds number based on the NGV chord length from 35,000 to 70,000 by doubling the mean inlet velocity does not change the breakdown behaviors of the investigated vortices' appearing. A possible explanation are the contrary mechanisms of increasing vortex swirl, axial velocity and adverse pressure gradient, whereas a higher swirl and pressure gradient moves the breakdown location further upstream and a higher axial velocity increases the distance from initiation to vortex breakdown.

7. CONCLUSION

This paper shows flow visualization pictures, a Strouhal number analysis of vortex breakdown phenomena and RMS signatures of the von Kármán vortex street in a turbine environment. These flow features are shown as they interact with the unsteady rotor pressure field. The breakdown of the horse shoe vortex pressure side limb seems to have a two stage behavior with an initial spiraling mode right after exiting the nozzle guide vane passage and other subsequent breakdown modes periodically occurring when interacting with the rotor pressure field and the von Kármán vortex street. An approach is presented that this over-all behavior does not depend on the Reynolds number at the Re level of the experiments.

To gain further insight into the behavior of vortex breakdown at increasing Reynolds numbers (i.e. increasing nozzle guide vane inlet velocity) in a turbine environment, Reynolds lapse analysis, experimentally as well as numerically, are required. For modern turbine stage designs with secondary vortices of low swirl, new analysis about reducing the axial gap for reducing vortex breakdown related losses has to be considered.

8. REFERENCES

[1] Gregory-Smith, D.G., et al., *Growth of Secondary Losses and Vorticity in an Axial Turbine Cascade.* Journal of Turbomachinery, 1988. vol. 110: p. pp. 1-9.

[2] Vogt, H.-F., *Wasserkanalversuche zum Einfluss der Schaufelform und Seitenwand auf die Sekundärströmungen in thermischen Turbinen.* Dissertation, 2006. Universität Stuttgart.

[3] Schlienger, J., et al., *Vortex-Wake-Blade Interaction in a Shrouded Axial Turbine.* ASME Turbo Expo 2004, 2004. ASME GT2004-53915.

[4] Göttlich, E., et al., *Investigation of Vortex Shedding and Wake-Wake Interaction in a Transonic Turbine Stage Using Laser-Doppler-Velocimetry and Particle-Image-Velocimetry.* Journal of Turbomachinery, 2006. Vol. 128: p. pp. 178-187.

[5] Marshall, J.S., *The Fluid Mechanics of Vortex Cutting by a Blade.* NASA, 1993. AD-A270 932.

[6] Squire, H.B., *Analysis of the Vortex Breakdown Phenomenon.* Part1. 1960, Aero. Dept., Imperial Coll.: London.

[7] Ludwieg, H., *Zur Erklärung der Instabilität der über angestellten Deltaflügeln auftretenden freien Wirbelkerne.* Z. Flugwiss., 1962. 10: p. 242-249.

[8] Lambourne, N.C., Bryer, D.W., *The Bursting of Leading-Edge Vortices: some Observations and Discussions of the Penomenon.* Aero. Res. Counc. R&M, 1961. 3282: p. 1-35.

[9] Faler, J.H., Leibovich, S., *Disrupted States of Vortex Flow and Vortex Breakdown.* Physics of Fluids, 1977.

[10] Sarpkaya, T., *Vortex Breakdown in swirling conical Flows.* AIAA, 1971. 45(3): p. 545-59.

[11] Binder, A., et al., *Unsteady Flow Interaction Caused by Stator Secondary Vortices in a Turbine Rotor.* Journal of Turbomachinery, 1987. Vol. 109: p. pp. 251-257.

[12] Kasper, C., et al., *A Study of Unsteady Secondary Flow in a Water Flow Axial Turbine Model*, in ASME Turbo Expo. 2008.

[13] Kasper, C., et al., *Water Flow Model Turbine Flow Visualization Study of the Unsteady Interaction of Secondary Flow Vortices with the downstream Rotor*, in *ETC*. 2009: Graz.

[14] Gallaire, F., et al., *Spiral Vortex Breakdown as a Global Mode.* Journal of Fluid Mechanics, 2006. vol. 549, pp.71-80. Cambridge University Press.

[15] König, M., Eisenlohr, H., Eckelmann, H., *The fine Structure in the Strouhal-Reynolds Number Relationship of the laminar Wake of a circular Cylinder.* The Physics of Fluids, 1990. 2: pp. 1607-1614.

[16] Abernathy, F.H., et. al., *Turbulence Spectra using Laser-Doppler Anemometry and selective Seeding*. In: Proc. of 5th Syrup. on Turb. 1977, pp.133-142.

[17] Escudier, M., *Vortex Breakdown: Observations and Explanations*, in Prog Aerospace Sci. 1988. pp. 189-229

[18] Leibovich, S., *The Structure of Vortex Breakdown*. Annual Reviews Fluid Mechanics, 1978. 10:221-46.

[19] Rockwell, D., *Vortex-Body Interactions*. Annual Reviews Fluid Mechanics, 1998. 30:199-229